

DINOv2 Rocks Geological Image Analysis: Classification, Segmentation, and Interpretability

Florent Brondolo^{1,*},[†] and Samuel Beaussant^{1,*}

¹Akkodis Research, florent.brondolo@akkodis.com,
samuel.beaussant@akkodis.com

[†]Project lead

*Equal contributions

Abstract

This study investigates the interpretability, classification, and segmentation of CT-scan images of rock samples, with a particular focus on the application of DINOv2 within Geosciences. We compared various segmentation techniques to evaluate their efficacy, efficiency, and adaptability in geological image analysis. The methods assessed include the Otsu thresholding method, clustering techniques (K-means and fuzzy C-means), a supervised machine learning approach (Random Forest), and deep learning methods (UNet and DINOv2). We tested these methods using ten binary sandstone datasets and three multi-class calcite datasets. To begin, we provide a thorough interpretability analysis of DINOv2’s features in the geoscientific context, discussing its suitability and inherent ability to process CT-scanned rock data. In terms of classification, the out-of-the-box DINOv2 demonstrates an impressive capability to perfectly classify rock images, even when the CT scans are out of their original training set. Regarding segmentation, while fast, thresholding and unsupervised methods perform poorly despite image preprocessing, whereas supervised methods show better results. We underscore the computational demands of deep learning but highlight its minimal intervention, superior generalization, and performance without additional image preprocessing. Additionally, we observe a lack of correlation between a network’s depth or the number of parameters and its performance. Our results show that a LoRA fine-tuned DINOv2 excels in out-of-distribution segmentation and significantly outperforms other methods in multi-class segmentation. By systematically comparing these methods, we identify the most efficient strategy for meticulous and laborious segmentation tasks. DINOv2 proves advantageous, achieving segmentations that could be described as ”better than ground-truth” against relatively small training sets. Code is available at <https://github.com/FloFive/DINOv2-X-Geosciences.git>.

1 Introduction

Digital rock physics is commonly used in various subsurface engineering fields such as Carbon Capture and Storage [48, 84, 49, 13], or Gas Storage [35, 43], which heavily rely on numerical analysis of physical and chemical properties of samples [41, 49, 26, 2, 71]. Central to this is micro-computed tomography (μ CT), a non-destructive imaging technique that offers invaluable insights into the internal structure and properties of geological formations at micron scales [65, 2, 10, 1, 49, 3]. This allows for investigations such as heterogeneities characterization, pore network properties, fluid flow studies or even contact angle measurements [65, 3, 13, 2, 88, 61, 11, 71]. Fluid injection and fluid mixing into rock samples can trigger changes within the rock fabric, including fracturing, dissolution, erosion, precipitation, and mechanical compaction. These processes induce micro- and macro-variabilities within the rock structures, potentially creating preferential flow paths that enhance fluid conductivity or, conversely, obstructing paths and disrupting fluid flow. As the need to understand subsurface integrity for projects like CO₂ storage grows, the importance of advanced vision algorithms to improve model-based studies becomes increasingly evident. Utilizing petrophysical models accelerates the qualification of subsurface sites and ensures standardization across qualification studies, promoting a systematic approach. In this context, high-quality segmentation masks of CT-scanned volume of rocks are crucial for such models [29, 1, 44, 40, 60].

However, translating μ CT data into actionable pore-scale modelling results through accurate image segmentation remains a labour-intensive, time-consuming, and subjective task [26]. To address these challenges, scientists often rely on machine learning or deep learning approaches for quick and precise segmentations. Yet, obtaining publicly available multi-class datasets that encompass a diverse range of rock types is particularly difficult. Moreover, deep learning approaches typically require a substantial number of training samples to perform and generalize well. Consequently, this scarcity of datasets prevents the research community from scaling and leveraging deep-learning-based geological segmentation models [17, 7, 26]. Therefore, the limited availability of data is a significant bottleneck for developing robust and versatile segmentation methods for Geosciences.

Despite these challenges, foundation models show the capability to perform effectively with minimal data, highlighting their potential to be more widely adopted in Geoscience applications. To the best of our knowledge, very few prior works explored and tuned foundation models to fit the specificity of CT-scanned rock samples. Meanwhile, foundation models are seeing a quick and widespread adoption within the Medical field [4, 19, 72, 28, 87, 93]. In this work, we assess the scalability of DINOv2 [69] for downstream applications. We hypothesize that such foundation models can be leveraged and applied to the Geoscience fields to perform accurate segmentation. We empirically check this assumption by comparing our method against a range of baseline models and traditional segmentation techniques [52] such as Otsu’s method [70, 54], K-means [42], fuzzy C-means [30, 8] (FCM), Random Forest [63, 55] (RF), two CNNs (a customized UNet [77, 53] and ResNet152 [34]). We opted for a challenging dataset characterized by high noise levels and limited data availability to explore the options available to researchers facing constraints in training capabilities, whether due to data scarcity or noise challenges.

This study highlights the need to utilize high-performing foundation models tuned to Geoscientific data for segmentation and classification, especially when faced with limited and varied training data. Our research shows the synergy between DINOv2 and Geosciences, demonstrating that DINOv2 significantly outperforms other widely used and popular segmentation methods. Notably, DINOv2 exhibits superior generalizing capability with noisy and scarce data, making it a powerful tool for advancing geological segmentation tasks. The goal of this research is to raise awareness amongst geoscientists regarding this powerful but underutilized vision model, as well as to provide empirical guidelines on how to best leverage it.

2 Background

The methods described in this section are popular segmentation tools that provide a fair trade-off between processing speed and segmentation quality. While they represent only a small subset of available algorithms, they serve as comparative benchmarks to highlight the capabilities of DINOv2. Segmentation techniques at the pore scale can be broadly categorized into several families, each with methodologies, use cases, advantages and limitations.

2.1 Threshold-based and unsupervised segmentation techniques

Unsupervised and threshold-based segmentation techniques are computationally efficient methods widely employed for image segmentation tasks. Despite their simplicity, they often struggle with complex and noisy data.

Among threshold-based techniques, the Otsu method, introduced by Nobuyuki Otsu [70], is notable. It has been adapted for multiclass problems [54] and is particularly effective in preserving details and edges in CT images [78]. The method determines the optimal threshold by maximizing between-class variance, ensuring optimal separation between foreground and background [92, 16]. Otsu’s method is widely used in various image processing applications, such as Fiji [79], but its performance in noisy environments is limited [16].

Unsupervised approaches like K-means and FCM do not require annotated data during training, learning directly from raw data. K-means partitions data into K clusters by assigning each pixel to the cluster with the closest mean intensity value [59, 82]. Despite its computational efficiency and ease of implementation [42], K-means may struggle with noisy data.

FCM, or soft K-means, allow data points to probabilistically belong to multiple clusters [30, 8]. This method is more robust than K-means in handling noisy data and overlapping clusters, providing

nuanced segmentation by considering the degree of membership to multiple clusters. This characteristic is especially beneficial in scan-type data and applications where boundary regions are ambiguous.

2.2 Supervised approaches

Two supervised techniques were chosen for this study. The first method is an adaptation of the RF algorithm, which is commonly employed in the WEKA segmentation tool of Fiji [79, 5]. On the deep learning front, after thorough consideration of various CNN-based approaches [26, 25, 53, 56], we opted for the UNet model introduced by [53]. This decision was influenced by factors such as task compatibility, IT constraints, and code availability. The UNet model was selected because its code is readily accessible and it has demonstrated strong performance in multi-class rock CT-scanning applications.

The RF algorithm [63, 55], is a versatile classification method that uses an ensemble of decision trees to improve predictive accuracy and generalization. Each tree is trained on a different bootstrap sample of the data, with randomness in both sample selection and feature choice, ensuring diversity among trees and reducing the risk of overfitting [55, 52]. Predictions in an RF are made by aggregating the votes from all trees, with the majority vote determining the final class. This approach leverages individual tree strengths while mitigating weaknesses, enhancing overall performance [63, 52]. Modern implementations, such as the WEKA trainable segmentation toolbox, enable parallel training of trees, significantly speeding up the process [5] while leaving the user in control of the features used for training the method. RFs have been successfully applied in various Geoscientific fields, including SEM image segmentation [89, 57, 52] and CT-scanned rock segmentation [74, 31].

The UNet architecture is a form of convolutional neural network (CNN) that can be used for image segmentation tasks. Introduced in [77], the architecture is characterized by its U-shaped structure, which consists of a contracting path (encoder) and an expansive path (decoder). The encoder captures the context of the input image through multiple layers of convolutional operations and downsampling [50]. This process extracts important features from the image, which in this context can be fractures, pores and mineral boundaries. The UNet architecture has demonstrated remarkable effectiveness in various segmentation tasks ranging from fracture segmentation [73] to mineral and petrological segmentation [52, 26, 83, 68, 53, 21] or even lithology identification [91]. While it has shown proficiency in these areas, the performance can vary depending on the availability and quality of annotated training samples. Nevertheless, they require training from scratch with extensive data, which is typically gathered, utilized, and safeguarded within the industry. The limited public datasets that do exist may face compatibility issues across repositories due to class imbalance and discrepancies in represented phases due to belonging to different projects. Overall, both UNet and CNNs have been instrumental in advancing the field of image segmentation, particularly in the context of digital rock analysis. Their ability to provide precise localization and accurate segmentation results makes them valuable tools for a wide range of applications.

2.3 The DINOv2 foundation model

Foundation models are large-scale, pre-trained models designed to serve as versatile bases for a wide range of downstream tasks. These models are exceptionally useful because they can be efficiently fine-tuned. Fine-tuning involves adjusting the pre-trained model on a smaller, task-specific dataset, enhancing its performance for that particular task. This approach often outperforms models trained from scratch, especially in scenarios with limited data. DINOv2 [69] represents a state-of-the-art self-supervised learning (SSL) method specifically designed for pre-training vision foundation models. It excels in creating robust image encoders by employing vision transformers (ViTs). These transformers leverage the attention mechanism [86], enabling the model to process images in a way that captures complex patterns and features. By pre-training this architecture on a vast and diverse dataset of images, DINOv2 generates visual features that are highly effective for various applications, such as image classification, object detection, and segmentation. Notably, DINOv2 models were primarily trained on "natural" images, depicting everyday scenes and objects. However, these models can be fine-tuned for more specific domains, allowing adaptation to specialized applications like Medical imaging or satellite image analysis [12, 6]. Overall, DINOv2 foundation models are pre-trained image encoders capable of extracting meaningful and robust representations from various types of images, making them suitable for a wide range of vision tasks.

3 Related works

The performance of deep learning models depends significantly on the size of the dataset and the model. Modern foundation models in natural image domains use millions of images and train models with hundreds of millions to billions of parameters [15, 75, 46, 69]. However, in specific scientific fields such as the Medical or the Geoscience domain, datasets of such scale are challenging to collect due to the frequency of image acquisition and data-sharing challenges. Understanding this, the DINOv2 model has gained significant popularity across various domain-specific fields due to its versatility and flexibility. Notably, it has advanced the state-of-the-art in complex vision tasks within the Medical field, including medical image analysis, computational pathology, and semantic segmentation. This widespread adoption underscores DINOv2’s adaptability and robust performance.

Recent advancements demonstrate that models trained on natural images can perform well on out-of-distribution OOD medical images. Foundation models like DINOv2 generate data representations that generalize well to various tasks, making them suitable for pathology, where data is often unlabeled and diverse applications are common. Amongst others, these tasks include general pathology, cancer detection, tumour profiling, biomarker evaluation, rare diseases, and even various tissue detection. These are done across various modalities (CT, MRI, Ultrasound) and anatomical regions, demonstrating effectiveness in jobs like localization, segmentation, depth estimation, and classification [87, 4, 28, 93, 24]. DINOv2 captures rich semantic features from images, enabling high accuracy and robustness in medical imaging tasks where detailed and accurate analysis is crucial [4, 6]. Several foundational models have been evaluated in studies [85, 9, 4, 39, 38], and DINOv2 has demonstrated superior adaptability to both in-distribution and OOD data. It generally surpasses methods such as stable diffusion, SAM, DINOv1, and the state-of-the-art UniverSeg [14] in a variety of segmentation tasks.

However, despite its success in the Medical field, DINOv2 remains underutilized in the Geosciences domain. This represents a promising opportunity to leverage its capabilities for segmenting CT-scanned rock images, potentially enhancing precision in rock segmentation which has been a pivotal task for many years. In the Geoscience domain, newly introduced foundation models have been largely underutilized. However, machine learning and deep learning approaches have been tested, starting with the well-known WEKA tool from the Fiji software [79, 5]. This tool, which is based on an RF algorithm, is widely used by the Geoscientific community. Many authors have presented various UNet and CNN architectures, either trained from scratch or utilizing pre-trained backbones to address this task, yielding satisfactory results [68, 83, 21, 52, 26, 91, 53, 62, 76, 64, 73, 56]. However, fewer studies have attempted to adapt large foundation models for Geoscientific segmentation tasks [81, 80, 47, 32, 45, 23, 37]. Notably, only one study has been identified using SAM for CT-scanner segmentation [58], and no studies have been found utilizing DINOv2 for this purpose.

4 Evaluation Settings

In this section, we briefly describe the experiments conducted to assess the potential benefits of DINOv2 in a Geoscientific context. We present the common settings used in our experiments, including the data used, the pre-processing pipeline and the values of some of the most significant hyper-parameters. Readers can refer to our publicly available code for more details and information. All experiments were run on an NVIDIA RTX 3060 and Tesla T4 GPU.

4.1 Motivations

The main purpose of our experiments is to analyse and highlight the strengths and limitations of DINOv2 within the very specific context of geological image analysis. In section 5, we conduct a comprehensive probing and interpretability analysis of DINOv2’s *raw* features (i.e. without any fine-tuning). Effective and powerful data representation abilities allow the model to capture the underlying structure of the data, which promotes better generalization and robustness. By examining how DINOv2 encodes rock data, we can gain a deeper understanding of the model’s innate suitability for the Geoscience domain. Additionally, high-quality features often correlate with efficient fine-tuning. Consequently, in section 6, we investigate the ability of a segmentation model leveraging DINOv2 to adapt to our application with minimal data. To better contextualize our performance metric, we

evaluate our model and provide a fair comparison with other SOTA approaches benchmarked in the same conditions.

4.2 Datasets

For this study, we utilize two distinct sets of CT-scanned data for separate analytical tasks. We refer to the classification dataset as the “sandstones” set and the segmentation dataset as the “carbonates” set. Each of the three calcite core samples from the carbonates set is respectively denoted by $S1$, $S2$ and $S3$. Each raw file is downloaded from public repositories and converted to TIFF format, and then to the NPY data format. We automatically adjust the brightness and contrast of the TIFF files using Fiji to improve the images, particularly given their rather dark appearance. This adjustment improves the sharpness of the features in the images, which in turn boosts our models’ predictions.

4.2.1 Segmentation task

For the segmentation task, the “carbonates” dataset consists of three CT-scanned calcite core samples, each with a diameter of 4.8mm and varying lengths [2]. These cores were extracted from different drilling surveys within the same reservoir rock in the Middle East and scanned using a consistent methodology as detailed by the authors. This dataset encompasses three classes: crude oil, brine, and rock matrix. While the researchers used a high-resolution beam to obtain these images, the CT-scans exhibit a high level of granularity, characterized by the visible grains, which are the smallest distinguishable parts of the image. However, the overall contrast of the image is relatively low, resulting in a minimal difference between some darkest areas. This low contrast makes it challenging to discern fine details within the rock’s structure. Despite these limitations, the texture of the rock’s surface is somewhat discernible, though the low contrast and resolution prevent the observation of finer details by eye only. These factors collectively impact the clarity and precision of the CT-scans, making detailed analysis of the rock’s microstructure more challenging.

4.2.2 Classification task

The classification task focuses on the “sandstones” dataset comprising 10 CT-scanned sandstone samples, each representing a different rock type with unique petro-morphological characteristics [67]. These CT-scans exhibit a noticeable level of granularity, although less pronounced compared to those intended for segmentation purposes. Each scanner captures distinct petro-morphological features, contributing to variations in contrast primarily influenced by particle sizes and their arrangement, resulting in a spectrum of gray shades. Although typically more interpretable, some scans may exhibit partial noise or artefacts. These characteristics are used for classification purposes in this study.

4.3 Data processing and augmentation

In deep-learning-based computer vision, it is frequent to perform data augmentation to improve model robustness and generalization. It is typically achieved with geometric and colour transformations such as rotations or colour jittering [69, 15] directly applied to the input data. Across our deep learning models, and unless otherwise stated, our transformation pipeline is composed of random or centre cropping, up-sampling, random vertical or horizontal flips, contrast, brightness and gamma adjustment. We experimented with multiple crop and up-sample sizes and found that a crop of size 224 followed by a bilinear up-sampling to 560 gave the best results. This resolution was selected after extensive trial and error, finding that larger resolutions improved results until we reached our computational limits. What seemed to emerge from these couple of trials is that fine-grained segmentation requires up-scaling relatively low-resolution images to extract high-quality features and bring out small but important stone details. For other approaches (machine-learning and threshold-based), we denoise the data with a non-local mean filter to improve robustness (no data augmentation involved). We also consider a hand-engineered basic feature extractor (BFE) to enhance some of our baseline machine learning algorithms (e.g. RF). It operates on denoised data and uses a Gaussian kernel to compute 15-dimensional feature vectors composed of pixel image intensity, gradient intensity, texture variations and local structure to capture features at different levels of detail, adapting to our needs what has been proposed in [89].

4.4 DINOv2 backbones and hyperparameters

Depending on the experiment, this study leverages three DINOv2 model sizes: DINOv2-small (22M parameters), DINOv2-base (86M parameters) and DINOv2-large (300M parameters), respectively displaying feature vector sizes of 384, 768 and 1024. Before being processed by the backbone, the input images are divided into fixed-size, non-overlapping patches. Following this, each of these patches is transformed into a corresponding feature vector using DINOv2’s ViT. All DINOv2 models were trained using a patch of size 14, which given our selected image size (560x560), yields feature patches of size 40x40 (560/14=40). Due to computational constraints, fine-tuning (or even inferring for DINOv2-large) the backbone was impractical with our available GPU resources. Therefore, we employ a parameter-efficient fine-tuning approach named Low-Rank Adaptation (LoRA) which efficiently adapts large models to specific tasks by significantly reducing the number of trainable parameters [36]. LoRA achieves this by freezing the weights of a pre-trained model to avoid retraining the entire model. Instead, it injects trainable low-rank matrices into some of the layers to approximate the changes needed for new tasks. Additionally, LoRA does not introduce extra inference latency, as the low-rank matrices can be merged with the pre-trained weights during inference. The rank of the LoRA matrices and the adapted layers are hyper-parameters that need to be tuned. In our case, we set the rank to $r = 32$ and target all the linear layers (including attention matrices). For instance, using DINOv2-base, we reduce the amount of trainable parameters, from 86M to only 5M, resulting in substantial computational resource savings. To further improve memory efficiency, we implemented 4-bit quantization. Quantization reduces the numerical precision of the model weights, thereby greatly reducing the memory footprint and computational requirements while maintaining the model performance. Combining quantization and LoRA fine-tuning (also known as QLoRA [27]) allows for memory-efficient fine-tuning and inference of large models without compromising the model’s accuracy.

5 Exploration of DINOv2’s understanding of rock CT-scans

Our first experimental studies focus on the interpretability of DINOv2’s features and their suitability to the Geoscientific domain. We leverage existing probing and visualization methods to inspect whether DINOv2 can natively recognize and discriminate important petrophysical patterns. In other words, we wish to understand how well DINOv2 “understands” CT-scans of rocks by scrutinizing the amount of useful information encoded in its features. Our experiments are based on two datasets, presented in section 4.2 with significantly different characteristics. Unless otherwise stated, all experiments are run using a non-fine-tuned (frozen) DINOv2, i.e. none of its weights are updated. By doing so, we highlight the intrinsic capabilities of DINOv2 as a backbone for OOD data.

5.1 Assessing DINOv2 for Rock Type Classification

5.1.1 Experimental sets

We visualize DINOv2-base features when fed with data from the sandstones dataset to gain some insights on the ability of DINOv2 to process CT-scanned data, while only considering an “out-of-the-box” DINOv2 model. We aim to discover if scanned rocks sharing the same geological nature possess close latent representations in DINOv2’s feature space. This would indicate a zero-shot geological pattern recognition ability. Since DINOv2 produces high-dimensional embedding vectors, we utilize t-SNE (t-Distributed Stochastic Neighbor Embedding) for visualization. This powerful machine learning algorithm excels in dimensionality reduction and is particularly effective for visualizing such data. Notably, t-SNE preserves the local structure of the dataset, making it invaluable for illustrating clusters and complex relationships within high-dimensional data. We further validate the capabilities of DINOv2 by training the k-Nearest Neighbors (kNN) model directly on top of the latent features to classify rock samples. Intuitively, if the t-SNE shows clean and distinct distribution of the data clusters in DINOv2’s latent space, we expect such a simple classifier to perform well. We randomly sample 3,000 images from the sandstones dataset and use a regular train/test split strategy, allocating 80% of the data for training and the remaining 20% for validation. We experiment with multiple values for the number of neighbours k and also vary the image resolution.

5.1.2 Results

We plot the t-SNE visualization of DINOv2-base’s features in Figure 1. As shown, scanners belonging to the same dataset (rock sample) are clustered together. More interestingly, rock samples sharing similar characteristics, such as Bandera brown and Bandera gray, also have close feature representations. The same phenomenon can be observed for Berea rocks. Qualitatively, one could also argue that Bentheimer and Bandera Gray stones are petro-morphologically dissimilar which may explain why their latent representations are so far apart (Cf. Figure 7).

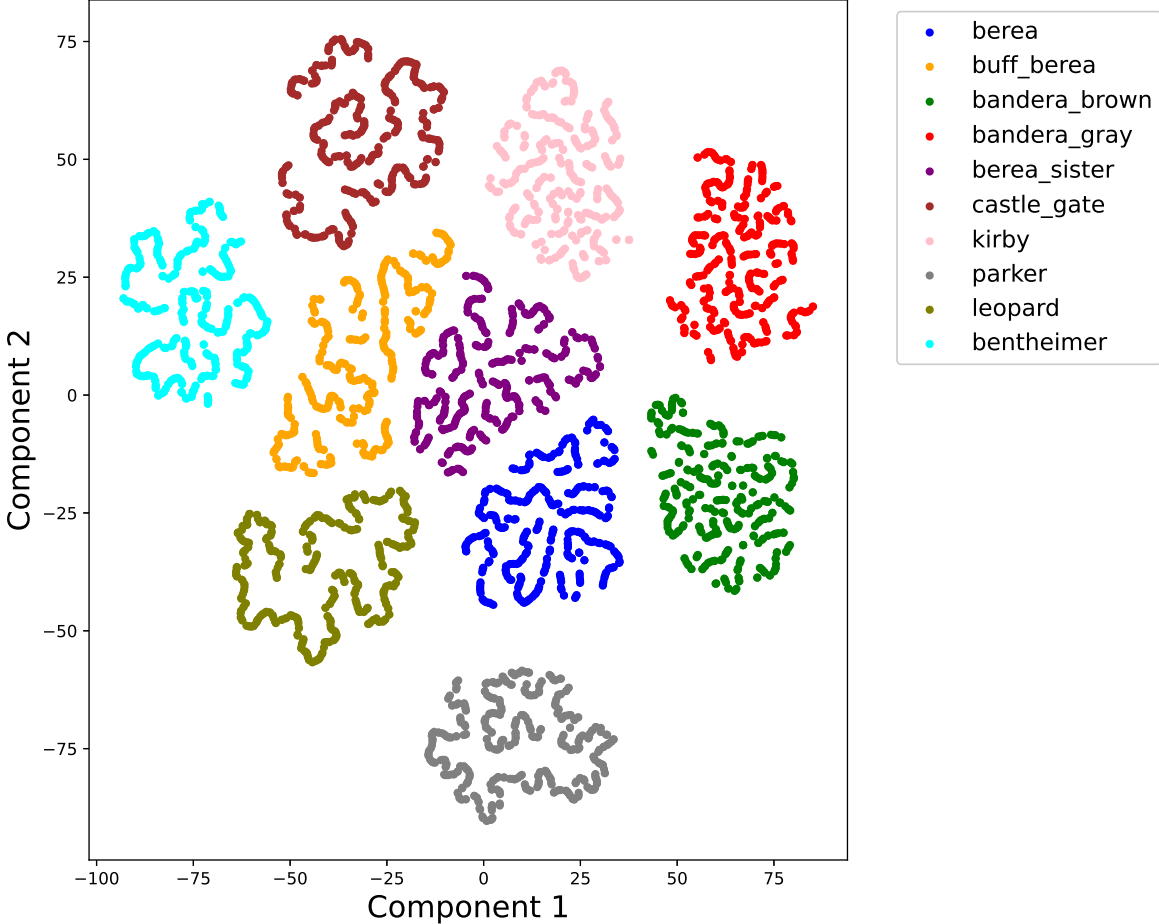


Figure 1: t-SNE visualization of the sandstones dataset embedded in DINOv2 feature space. This figure shows a 2-dimensional representation of DINOv2 clustering for the different rock samples.

Regarding rock classification with a kNN model, results are largely stable with respect to the number of neighbours k and the image resolution. Except for very low image resolution (below 128x128) or very high values for k (above 100), classification accuracy reaches 100%. Outside of these ranges, we observed classification accuracy that decreases down to 96.5%.

Overall, these first experimental cues validate that DINOv2 is sensitive to subtle but discriminating rock features despite having never been trained on this precise domain. As shown from the t-SNE plot, its feature space can be interpreted well and has a meaningful structure, leading to a perfect classification score with a simple kNN model.

5.2 Linear and kNN probing for segmentation

We extend our previous findings and further study the performance of DINOv2 on a more challenging image segmentation task.

5.2.1 Probing for feature quality assessment

When tackled with deep learning, pixel-wise classification usually requires specialized and sophisticated neural network architectures [26, 25, 53, 22, 90]. Instead, we rely on a simple linear classifier fitted on top of an “out-of-the-box” DINOv2 encoder. This linear layer decoder evaluation is used to isolate the performance of DINOv2 from the added contribution of a potentially powerful segmentation head. Indeed, a well-structured representation space effectively captures the underlying structure and relationships of the data, facilitating tasks such as classification and clustering. As such, and under this experimental setting, linear classification accuracy can be used as a proxy to assess the quality of a considered feature space given a frozen backbone. This simple procedure is called *probing* and is widely adopted in SSL [15, 69, 33, 20] to quantify the usefulness of features extracted by a pre-trained model for downstream tasks. For the same reasons, we also fit a kNN model for segmentation and perform kNN probing.

5.2.2 Experimental settings

We experiment with DINOv2-small, DINOv2-base and DINOv2-large to study how the feature size correlates to downstream performance. Additionally, we report probing results on the features extracted by BFE (see Section 4.3) to highlight the benefits and overall superior quality of the features learned by DINOv2. For linear probing, the segmentation head consists of a single convolution layer with a 1x1 kernel and no padding. It is applied to the feature map to predict class logits. For DINOv2, the 40x40 logits map (see Section 4.4) is then bilinearly upsampled to the full resolution (560x560). As in the original DINOv2 paper [69], we consider a boosted version of the linear probing setup in which we concatenate the patch tokens of the 4 last layers of the backbone before the classifier. For kNN probing, the feature map is upsampled from the low-resolution 40x40 feature map to a higher resolution that matches the ground-truth masks (GT). This ensures a one-to-one mapping between the training labels and feature vectors. kNN models scale poorly with the number of pixels because their computational complexity increases significantly with larger datasets. This is due to the need to calculate distances between each point in the dataset. To address this, we upscale DINOv2 features from 40x40 to 128x128 and downscale the GT masks from 224x224 to 128x128, making prediction computationally feasible on our hardware, while rendering large enough images. For the same reasons, we use only 200 images for training and evaluate on 100 images. During prediction, pixel-wise classification is performed by extracting features from the test images and finding the k-nearest pixel’s latent representations in the training set, along with their corresponding labels. In practice, we found that $k = 50$ neighbours gave the best results.

5.2.3 Results

We perform linear and kNN probing for multi-class image segmentation on the carbonates dataset. For this setup, we train our model on samples $S1$ and $S2$, and report the model’s performance and generalization ability using the IoU metric on the held-out and unseen $S3$ data subset. Results are reported in table 1. As shown, DINOv2 probing significantly exceeds the performance achieved using a regular feature extractor. Interestingly, the kNN and linear classifier, trained on top of a BFE, perform poorly and thereby indicating that this pixel classification task is not trivial. By contrast, this shows the essential contribution of DINOv2’s powerful features to its success on the task. A sample of the predicted segmentation mask for both methods is available in Appendix A.

We use t-SNE visualisation to comprehend why kNN works well coupled with DINOv2 compared to BFE. We plot the low-dimensional representation of each 128x128 feature vector, for the same image and both approaches in Figure 2. It appears that the feature representation of the tested image under BFE is much more disorganized than DINOv2’s. With BFE, the pixel’s feature representation corresponding to the brine and the rock matrix are mostly blended and overlap each other. This can be qualitatively observed in Figure 10 in Appendix A which depicts a predicted mask with a kNN and BFE. Quantitatively, as shown in Figure 3b which displays the confusion matrices for both DINOv2 and BFE representations, a significant amount of pixels from the brine class (79.5%) are incorrectly classified as pixels corresponding to rock matrix. In contrast, pixels representing crude oil are better clustered in the t-SNE plot, explaining why they are classified with more accuracy. In DINOv2’s case, the latent space contrasts the 3 classes much more efficiently leading to a better probing

performance. Nevertheless, there are still overlaps between some instances, explaining the confusion and misclassification of some pixels (see Figure 3a for more details).

Models	kNN	Linear	
		1 layer	4 layers
DINOv2-small	0.584	0.584	0.701
DINOv2-base	0.617	0.663	0.732
DINOv2-large	0.621	0.673	0.730
BFE	0.451	0.387	

Table 1: Segmentation results with probing on the test dataset measured as the IoU.

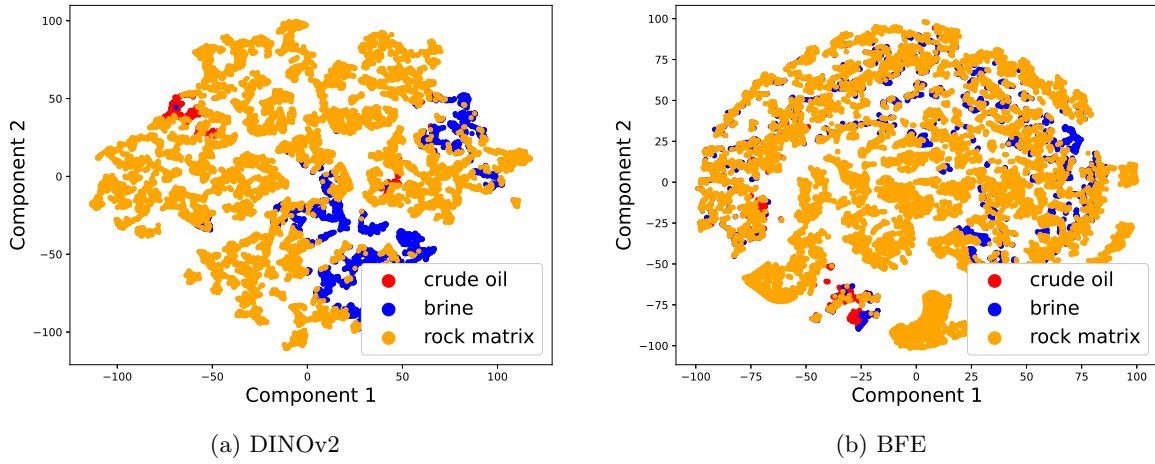


Figure 2: t-SNE visualization of pixel-level feature vectors for a test image from sample *S3*. This figure shows a 2-dimensional representation of DINOv2 and BFE clustering the pixel’s latent representation of the same image.

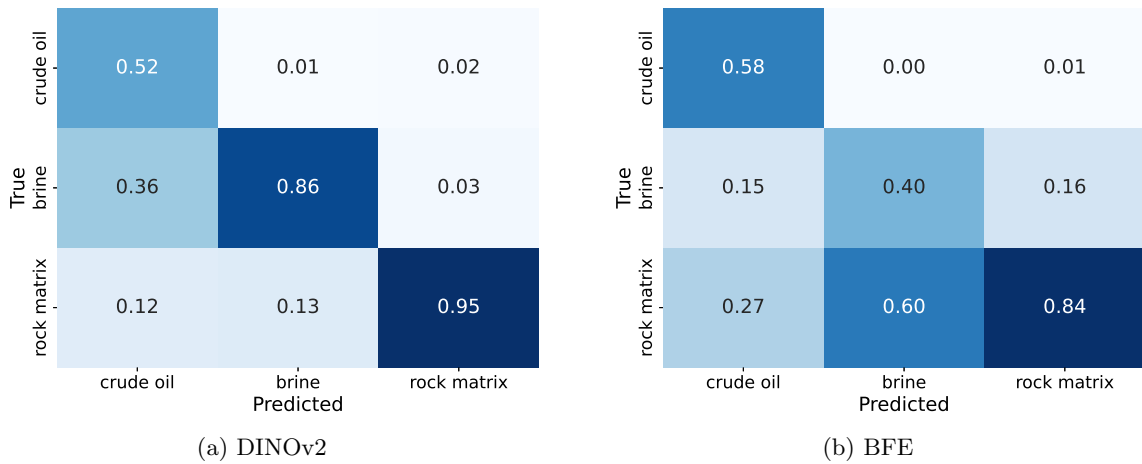


Figure 3: Confusion matrices for a segmentation prediction with kNN probing on a test image. Row indices of the confusion matrix correspond to the true class labels and column indices correspond to the predicted class labels.

From a performance perspective, the boosted linear probing setup, which processes the last 4 layers of DINOv2, significantly outperforms its 1-layer counterpart and the kNN classifier, especially for DINOv2-small (+0.117 IoU). This implies that useful information is also included in the intermediate layers, not only in the final layer. However, the performance gain from processing multiple layers decreases as we increase the feature size, for example, it only results in +0.057 IoU for DINOv2-large. This is likely because higher dimensional features can intrinsically embed more information, thus adding too many layers can be redundant. Furthermore, processing more features inevitably involves more computations. Therefore, and in practice, the number of processed layers can be treated as an extra hyper-parameter to trade off computation cost and performance. It is also worth noting that for large feature dimensions (≥ 768), linear probing achieves better IoU results than kNN which works poorly with high-dimensional data.

Overall, we found that a simple linear classifier trained on top of the frozen DINOv2’s features achieves impressive results in a segmentation task compared to a hand-engineered BFE. Moreover, DINOv2 has shown remarkable robustness to noise compared to BFE-based models which required an additional data denoising step. When fed with multi-layer features, it even comes close to a fully supervised UNet model trained from scratch (0.78 IoU) specifically on this task and this dataset. Moreover, the t-SNE visualization provides a nice way to interpret DINOv2’s features and explain its surprising zero-shot generalization to geological data. Yet, DINOv2’s performance can still be drastically improved with a parameter-efficient fine-tuning technique and a more sophisticated segmentation head (see Section 6).

5.3 PCA visualization of DINOv2 features

5.3.1 Experimental sets

Prior research on self-supervised vision foundation models has demonstrated the emergence of properties such as semantic segmentation [15, 69], despite the models not being explicitly trained for specific tasks. However, these phenomena have been observed primarily in natural images that are close to the training distribution. The question remains whether these spontaneous abilities extend to Geoscientific data. Following the original DINOv2 publication [69], we compute the Principal Component Analysis (PCA) on the features predicted by DINOv2-base for CT images to investigate this matter. PCA is a dimensionality reduction technique that transforms high-dimensional data into a lower-dimensional space by identifying directions of maximum variance. We display the first three principal components by assigning each to a different colour channel, creating a visual representation where similar parts are shown in matching colours. To improve interpretability, we apply a threshold to the first principal component, if necessary, to remove small outlying regions.

We consider two settings: a non-fine-tuned DINOv2-base and the same model after fine-tuning. The non-fine-tuned setting enables us to visualize the extent to which spontaneous segmentation emerges with rock data. In contrast, the fine-tuned backbone helps us understand how the features evolve after task-specific training. Fine-tuning is performed using QLoRA, and a linear segmentation head which incentivizes the model to rely as much as possible on the backbone. In Figure 4, we illustrate PCA on the same 2D slice of rock from the carbonates dataset for both models.

5.3.2 Results

We observe a clear difference between Figure 4b and Figure 4c. The out-of-the-shelf DINOv2 outlines the most salient parts of the image but fails to segment the different phases (oil, brine and rock matrix). Indeed, it seems to focus on shapes and surfaces but mostly disregards their semantic characteristics. We interpret this as evidence that CT-scans of rock samples represent significant OOD data for the DINOv2 model. As such, non-fine-tuned PCA features do not exhibit spontaneous and meaningful segmentation masks, in contrast to in-distribution natural images. However, the fine-tuned features displayed after a PCA accurately target three different classes as displayed in Figure 4c: crude oil (purple), brine (yellow) and the rock matrix (dark blue).

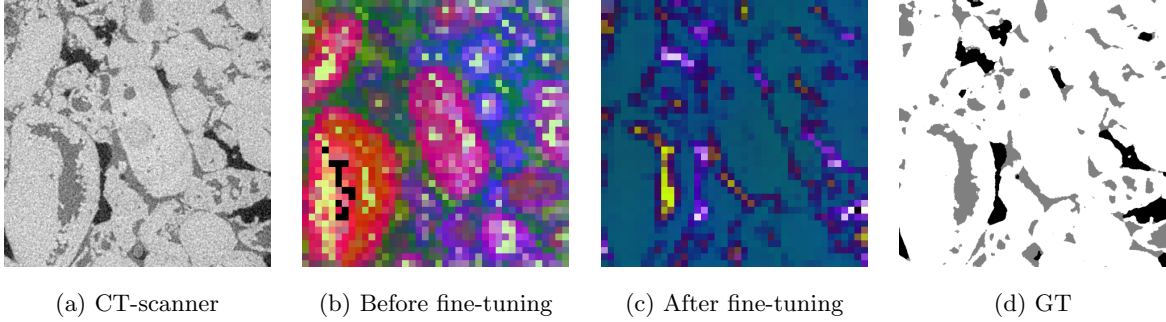


Figure 4: Visualization of the 3 principal components of CT-scanned images respectively using the raw features of DINOv2 (b) and using a fine-tuned linear head (c). The CT-scanner (a) and the GT (d) are displayed for easy comparison.

6 Fine-tuning DINOv2 for high-quality segmentation

In this section, we focus our empirical analysis on the performance of DINOv2-base segmentation models after fine-tuning on the carbonates dataset. To better understand the contribution of each part to the overall performance, we first conduct an ablation study on our proposed model. Following this, we benchmark our best-performing variant against multiple widely used SOTA segmentation techniques for rock CT-scans to determine how it compares performance-wise. In particular, we adopt an experimental protocol that assesses the ability of tested models to learn and generalize from potentially small amounts of noisy data. By doing so we closely mimic the more realistic and practical conditions which researchers can face.

6.1 Ablation study

6.1.1 Experimental settings

For both experiments, we train on the samples $S1$ and $S2$ datasets, and validate performance using the IoU metric on the held-out sample $S3$. All experiments are run using the DINOv2-base backbone as it represents a good trade-off between computation cost and performance. In addition to our linear head (same as in our linear probing setup in Section 5.2), we consider a 4 convolution layers segmentation head (which we refer to as ConvHead). The segmentation head starts with an initial convolutional layer that reduces the input features to 512 channels, followed by 4 decoder layers that progressively upscale and apply convolutions, with Leaky ReLU activation and dropout applied every two layers. The final segmentation map is produced by a convolution layer reducing the channels to the desired number of output classes. Each convolution layer uses a 3x3 kernel with padding set to “same”. We converged to this architecture with manual hyper-parameters search and some insights from section 5.3. As shown in Figure 4c, a PCA can extract an accurate (but low-resolution) segmentation mask from a fine-tuned backbone. Since PCA is a linear projection, we hypothesize that a simple segmentation head should work well. Experimentally, we found that overly powerful segmentation heads, such as UNets decoder or even simply 4 CNN layers with non-linear activation functions, lead to strong over-fitting. This is further corroborated by prior work [39] that found linear head to work better than transformer-based segmentation head. As a result, we strived for the right balance between simplicity and modelisation power. We consider 4 segmentation models based on DINOv2 depending on whether we fine-tune the backbone and which head is trained on top:

- **DINOv2-LinearHead:** The same model used for the linear probing (see Section 5.2). This baseline set provides insights into the intrinsic abilities of DINOv2 on rock segmentation.
- **DINOv2-LinearHead-FT:** A DINOv2 fine-tuned with a simple linear classifier simultaneously trained on top. As such, the segmentation performance heavily relies on DINOv2’s adapted features.
- **DINOv2-ConvHead:** An “out-of-the-box” DINOv2 backbone with a ConvHead fitted on top of the frozen features. This is used to identify the impact of a more powerful segmentation head

independently from a fine-tuned backbone.

- **DINOv2-ConvHead-FT**: The full model where the backbone is fine-tuned in conjunction with a powerful segmentation head.

Fine-tuned models are 4-bit quantized and fine-tuned using LoRA. We also consider 3 other baselines to better contextualize IoU performances: a light-weight UNet (UNet-small) with roughly the same number of trainable parameters as DINOv2-LH-FT (respectively 7.8M and 5.3M), a large UNet (~ 31 million parameters) and a QLoRA fine-tuned ResNet152 encoder with a ConvHead. We conducted experiments on these models while maintaining consistent hyperparameters (see Section 4.3). Each network is trained over 20 epochs and with 1000 images, evenly sampled between samples *S1* and *S2* from the carbonates set 4.2. For the large UNet model, we reduced the batch size from 15 to 8 due to GPU RAM limitations.

6.1.2 Results

Figure 5 displays the mean IoU achieved after 5 runs for each model using exactly 1000 images of size 560x560 for training (from *S1* and *S2* samples). As shown, DINOv2-LinearHead still outperforms a LoRA fine-tuned ResNet152 despite its significantly lower trainable parameters count. Indeed, the ResNet152 was pre-trained on a standard supervised classification task which likely produces over-specialized features, harder to adapt to OOD data and unseen tasks. As expected, selecting a more sophisticated segmentation head on top of DINOv2’s frozen features notably improves IoU performance (0.75 against 0.67) and is competitive with our UNets baselines. However, the biggest performance boost comes from fine-tuning the DINOv2 backbone with LoRA. In this setting, a simple linear head is still enough to reach 0.8 IoU, outperforming both UNets trained from scratch, underscoring the usefulness of DINOv2’s features. Interestingly, only a small improvement is observed when transitioning from DINOv2-LinearHead-FT to DINOv2-ConvHead-FT, suggesting that most of the overall performance can be attributed to the fine-tuned backbone. We also note that increasing the parameter count of our UNet model from 7.8M to 31.3M does not improve performances and even leads to slight overfitting.

6.2 Benchmark

We evaluate the segmentation performance of every benchmarked model under different data regimes. The reader can refer to 2 for a review of the evaluated methods.

6.2.1 Experimental settings

Each supervised model is trained on the carbonates dataset described in Section 4.2, using a varying number of images, from 4 (2 images per sample) to 1200 (600 images per sample). The training set consists of sample *S1* and *S2*, while testing is performed on sample *S3*. For segmentation methods that do not require training (Otsu, K-means, and FCM), inference and evaluation are conducted solely on sample *S3*. This approach is based on our objective to achieve the best possible segmentation on *S3*, as defined by the task requirements. For the supervised models, we selected the two models with the highest IoU scores from among the UNets and DINOv2 variants: the DINOv2-ConvHead-FT model and the lightweight UNet, as discussed in Section 6.1. Additionally, we included a RF model in the benchmark, chosen for its strong performance in the high-performance WEKA tool of Fiji [79]. The hyper-parameters of the RF model were optimized using a grid search. Instead of using raw pixels as input, we enhanced the RF model by feeding it features extracted by the BFE from Section 5.2, thereby improving its performance and robustness.

6.2.2 Results

The three unsupervised segmentation algorithms (Otsu, K-means, and FCM) report satisfactory and similar results on *S3*, with IoU values of 0.672, 0.672, and 0.67, respectively. Before segmentation, all images processed by these methods were denoised using a non-local means filter, as using raw images resulted in significantly lower IoU values.

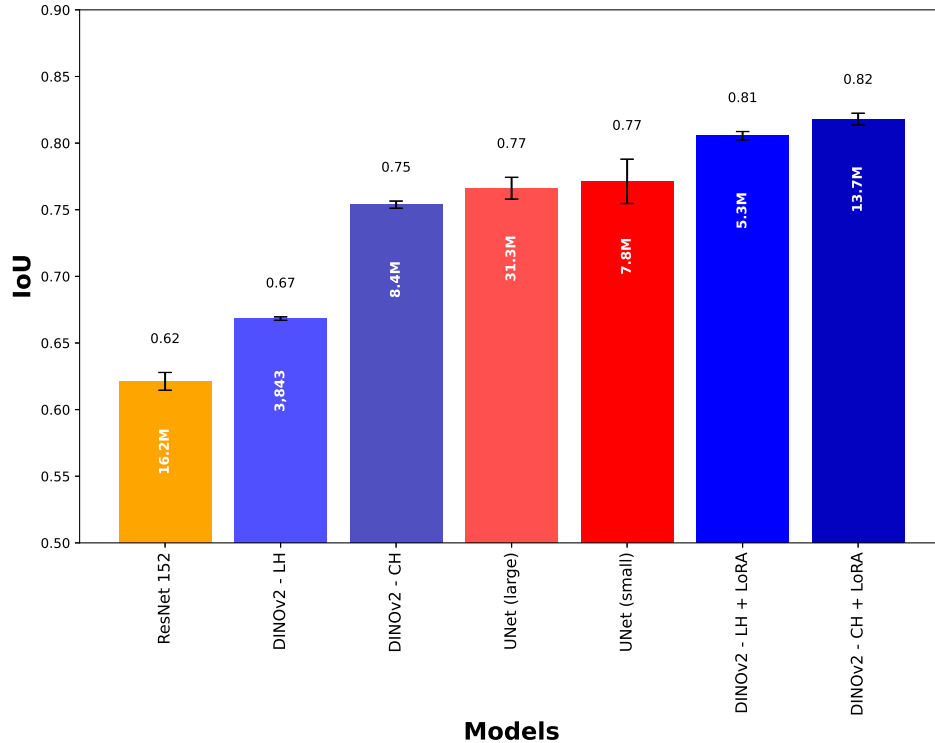


Figure 5: IoU values for various models and heads. Models compared are ResNet152, UNet and DINOv2. Heads are the linear head (LH) and the slightly more complex ConvHead (CH). The values in each bar show the number of trainable parameters per model.

We report the evolution of the IoU metric for each tested supervised model as a function of the amount of data injected into the model during training (Figure 6). Readers can refer to Figure 11 in appendix B for quantitative results. It is important to note that, in this phase, we are performing training using raw data (no denoising). As discussed previously, DINOv2-ConvHead-FT significantly outperforms our best UNet model even in relatively “high” data regime (above 1000 training images). The performance gap widens rapidly as we decrease the amount of training examples. While DINOv2-ConvHead-FT retains most of its performance until 200 training images, the UNet’s IoU notably degrades, dropping from 0.78 to 0.65 with 200 training images, which is equivalent to a 17% drop. This disparity becomes even more pronounced in an extremely limited data regime (below 100 training images) as the UNet significantly overfits to the few training samples available, leading to a catastrophic fall in performance (up to 50% loss at 4 images). Impressively, our DINOv2 segmentation model manages to achieve 0.74 mean IoU with as few as 4 training samples for fine-tuning, a performance comparable to a UNet trained from scratch with 1000 images. Regarding the RF model, it performs remarkably steadily across all data regimes but achieves lower IoU performance than DINOv2-ConvHead-FT. However, it outperforms the UNet model when trained with 500 data points or less. This illustrates well the trade-off between classical machine learning algorithms and deep learning. While the former is intrinsically limited by its simplicity but does not require large amounts of data to perform well, the latter can learn complex tasks but is very data-hungry. Given our results, it seems that DINOv2 exhibits the generalization capabilities of robust but simple machine-learning algorithms while retaining the modelling power of deep-learning-based approaches. Overall, DINOv2-ConvHead-FT achieved the highest IoU scores across all data regimes which emphasizes the strong generalization and adaptability of DINOv2 as a backbone.

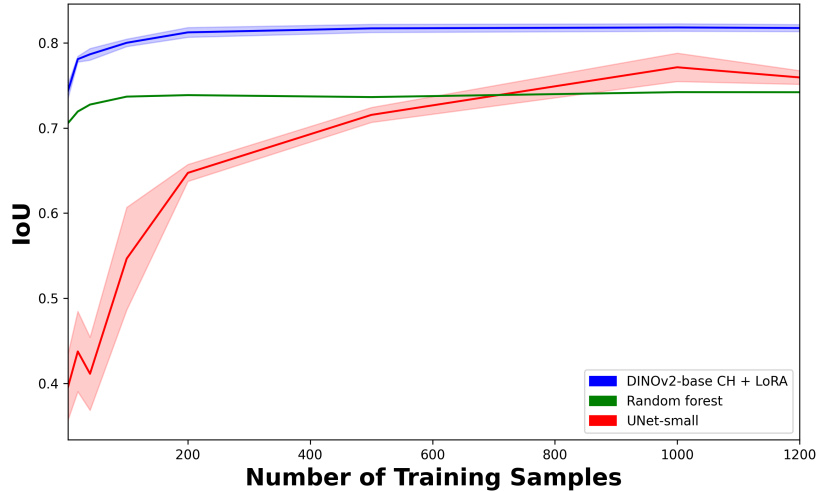


Figure 6: IoU as a function of the number of samples used during training of RF, UNet-small and DINOv2.

7 Discussion

In our study of DINOv2’s classification capabilities on the sandstones dataset, we found evidence of its capability to distinguish geological patterns based on latent representations. The t-SNE visualization of DINOv2’s feature space illustrated cohesive clusters corresponding to samples from the same geological dataset, affirming the model’s ability to capture and represent geological similarities. Notably, samples with similar petro-morphological characteristics exhibited proximity in the feature space, indicating DINOv2’s capability to generalize across subtle geological variations. While it is generally unclear what the components are in such analyses, by plotting a zoomed-in crop of a representative 2D slice of each dataset, centred around the barycenter of their respective point cloud, we can analyze what visual characteristics are observed as meaningful in the repartition of geological scanners (cf. Figure 7). In that matter, the first component seems to approach the size of the pores, while the second component might focus on the density of the porosity. While this observation has only been centred on a similar set of data, it highlights 1) the strength of a non-fine-tuned DINOv2 being able to meaningfully organize geological datasets by petromorphological traits, and 2) the potential of using DINOv2 as a powerful tool for uncovering underlying geological features and patterns that may not be immediately apparent through traditional analysis methods. These findings highlight the model’s capacity to interpret complex geological features effectively for accurate classification tasks, despite being pretrained on unrelated data. Such adaptability and interpretability not only enhance its utility in geological analysis but also extend its potential for diverse applications in pattern recognition across various domains.

Previous results have demonstrated the superiority of segmentation models leveraging DINOv2’s performance over other supervised approaches, such as UNet and RF, or even more traditional methods like Otsu, K-means or FCM. One of the primary experiments in this study involved segmenting a sample (*S3*, see Section 4.2). While supervised methods were trained using two similar samples (*S1* and *S2*), we aimed to compare more traditional approaches (Otsu, K-means, and FCM) based on their IoU performance. The traditional methods demonstrated suboptimal results in segmenting *S3*, despite achieving relatively high IoU scores on *S1* and *S2* (greater than 0.79 and 0.69, respectively). Although *S3* exhibited intrinsic characteristics similar to those of *S1* and *S2*, it posed significant challenges to the traditional methods. This observation suggests that, despite their effectiveness on most datasets, these traditional segmentation methods can encounter limitations and difficulties, even when dealing with ostensibly similar data.

On the supervised front, the results were variables. By looking at Figure 8 which displays the confusion matrices for the three above-mentioned models, we find that the rock matrix class, which

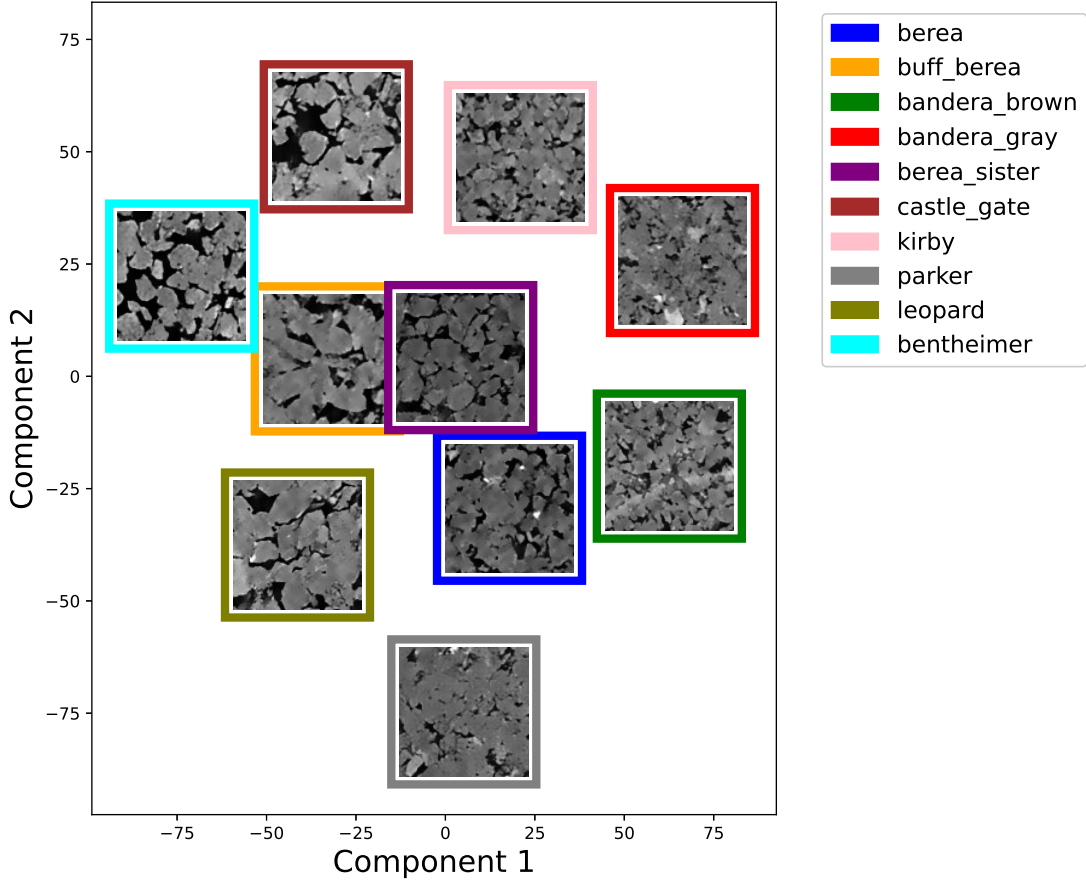


Figure 7: t-SNE visualization of the CT-scanner images of sandstones dataset embedded in DINOv2 feature space. This figure shows a 2-dimensional representation of DINOv2 clustering for the different rock samples, each represented by one 2D slice.

was the most prevalent, is generally the easiest one to get classified across all models. However, the brine and crude oil classes, which are under-represented with only 12.66% and 2.41% representation respectively, pose significant challenges. Our results reveal that the DINOv2 model outperforms all other models, demonstrating an impressive ability to correctly classify 89% of the brine and 72% of the crude oil pixels. This performance is particularly remarkable considering the under-representation of these categories, alongside the high granularity and low contrast present in the images (Cf. Section 4.2). In contrast, the UNet and RF models experience difficulties in segmenting the crude oil class, only achieving 42% and 55% accuracy respectively. This discrepancy in performance underscores the superior generalization capability of the DINOv2 model, especially in handling under-represented classes. However, specialized foundation models for segmentation such as SAM were not considered. Despite prior studies concluding that DINOv2 outperforms SAM in segmentation tasks, it has not been yet confirmed that this also holds for rock segmentation. We leave this for future work.

It is also worth noting that we did not push the architecture of our DINOv2 segmentation model to its limits as there is still potential for further improvement. For instance, from the experiment in Section 5.2, performance seems to correlate with feature size. As such, one could fine-tune and use a larger DINOv2 backbone if computation resources allow it. Additionally, a more sophisticated model architecture could also bring significant performance benefits. A better architecture might involve a pre-trained ResNet encoder feeding DINOv2 and a UNet-like decoder with skip connections, as described in the TransUNet architecture [18], allowing the segmentation head to capture more details. Concatenating features from intermediate layers of the DINOv2 backbone may also improve results considerably as shown in Table 1.

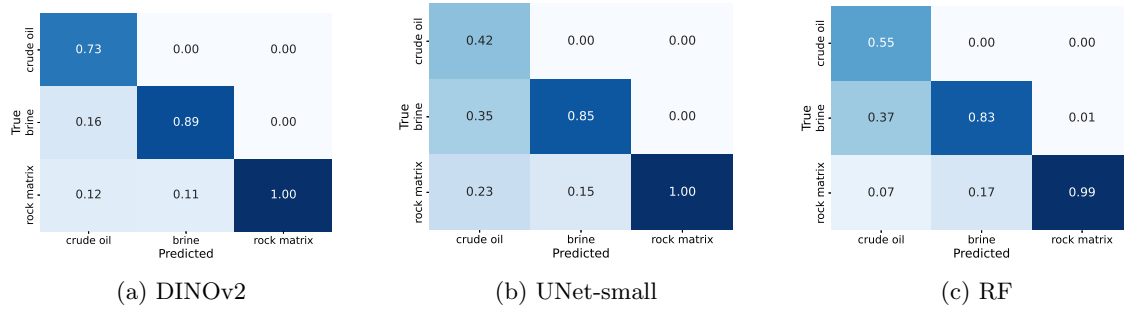


Figure 8: Confusion matrices for the segmentation predictions on sample *S3*, trained with 500 images as inputs, for each benchmarked model.

However, finding the best DINOv2 architecture was not the focus of this study. Instead, we opted to highlight the numerous advantages of using DINOv2 for computer-vision-related tasks for Geosciences.

We also reflect on the reliability of the GT used in this study. Indeed, despite achieving the best IoUs using DINOv2, it is important to wonder whether this translates into an accurate physical model. As previously noted in studies [53, 26, 73], the labels used for the segmentation workflow are never perfect. As such, the IoU metrics quantify the agreement between the predicted labelled images and the GT, rather than the exact distribution of the minerals. We found that DINOv2’s predicted labels even outperform the training labels in certain situations (Figure 9). Moreover, the segmentation results from the DINOv2 model can be less affected by human subjectivity, which is a significant advantage for reliable physical properties estimation in a systematic study such as those involving binary and/or multi-class segmentation of rock CT-Scanner [53].

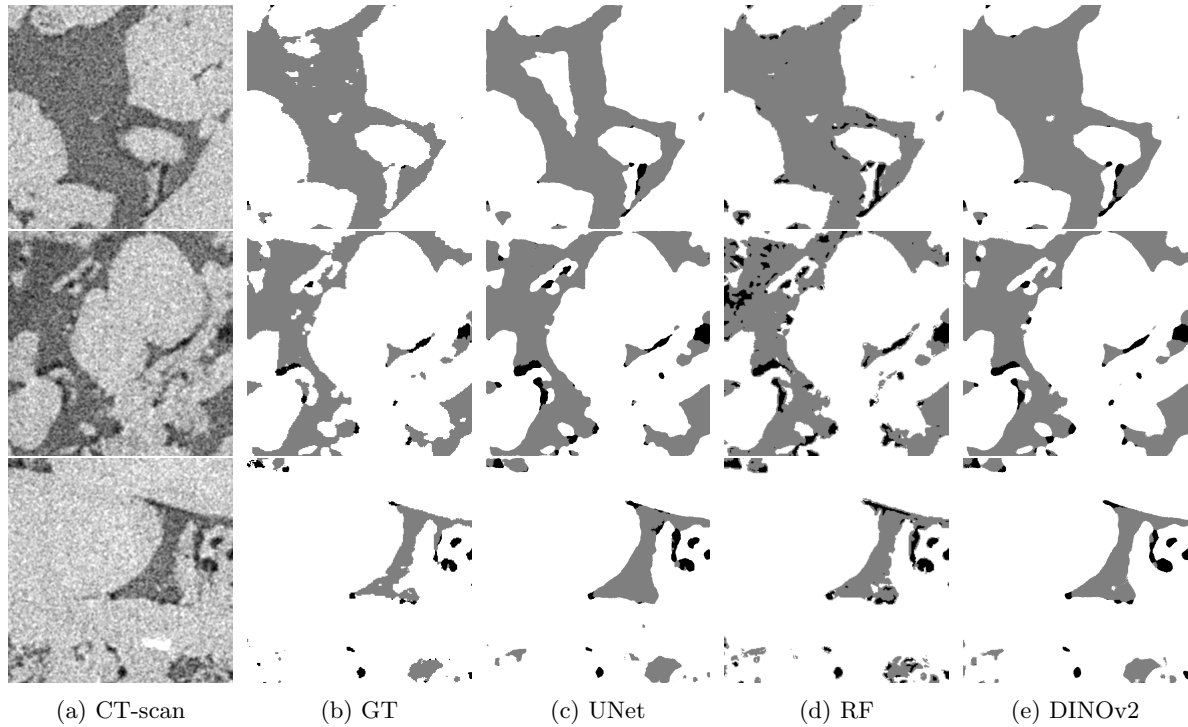


Figure 9: Predicted masks for the UNet model, the RF and our DINOv2 segmentation models for three different scanners with low-quality GT.

8 Conclusion

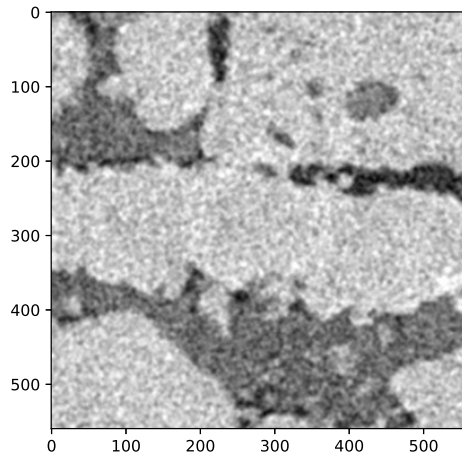
In this study, we thoroughly examined the applicability of DINOv2 for the segmentation of μ CT-scanned rock. Our goal was to assess the effectiveness and adaptability of a DINOv2-base model in the context of geological image analysis. Through extensive probing and visualization, we confirmed that DINOv2’s features could effectively capture and discriminate subtle geological patterns, leading to accurate classification and segmentation tasks. Impressively, linear and kNN probing on DINOv2’s features demonstrated significant performance improvements over BFEs, with DINOv2 achieving near-supervised performance without any fine-tuning. Moreover, our t-SNE visualizations and PCA analyses provided valuable insights into the model’s inherent ability to understand and represent geological data and informed our design of a suitable segmentation head. Indeed, our fine-tuning experiments validated that a relatively simple segmentation head, combined with the fine-tuned DINOv2-base backbone, could achieve superior segmentation accuracy compared to more complex models like UNet and ResNet152. When benchmarked against popular segmentation methods such as Otsu thresholding, K-means, FCM, and RF, DINOv2-base models consistently outperformed these approaches across various data regimes. Particularly in low-data settings, DINOv2’s performance remained robust, highlighting its potential to overcome common limitations in geological image segmentation, such as data scarcity and noise. It was also shown to be less affected by class imbalance than other baselines, enhancing its practical benefits. Overall, these findings underscore the efficiency of DINOv2’s feature representations and its potential for improving segmentation performance in the highly specialised Geoscientific domain.

However, several unresolved questions persist, leading to new research directions. Investigating hybrid models that combine DINOv2 with other advanced segmentation architectures, such as TransUNet, could achieve even higher performance. Similarly, we did not consider sophisticated fine-tuning and domain adaptation approaches that might further improve performances. For instance, generating additional synthetic data and targeting the most sensitive layers to the distribution shift, as explored in [51, 66]. Moreover, this study focused on the DINOv2 foundation model, a generic vision model. Finally, addressing the issue of unreliable GT labels is also a promising direction for future work. One could leverage robust training approaches to improve generalization capabilities even with noisy labels. On a similar topic, assessing the physical accuracy of predicted masks depending on the segmentation approach is also of interest. We believe that DINOv2 has the potential to significantly improve geological image analysis due to its robustness in both high, low and noisy data regimes, coupled with its SOTA performance. We hope that our study sheds some light on this powerful, yet highly underused tool by the Geoscientific community, and will help future geological research and practical applications.

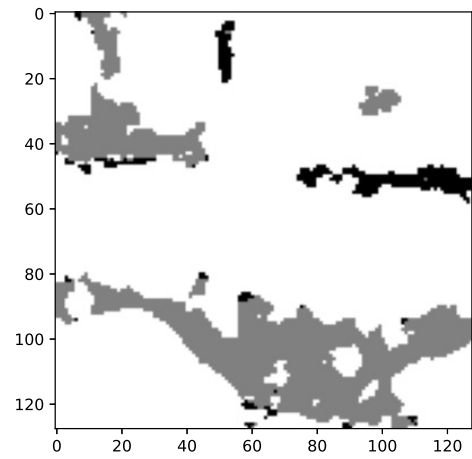
Acknowledgment

This research was funded by the Akkodis Group as part of the Semantic Classification of High-resolution Imaging for Scanned Materials (SCHISM) project. This study is an integral part of the SCHISM project, which is incorporated within the "Decarbonized Industry" innovation line of Akkodis Research. The project aims to explore and develop innovative solutions for CO₂ management and storage, contributing significantly to the decarbonization of industry.

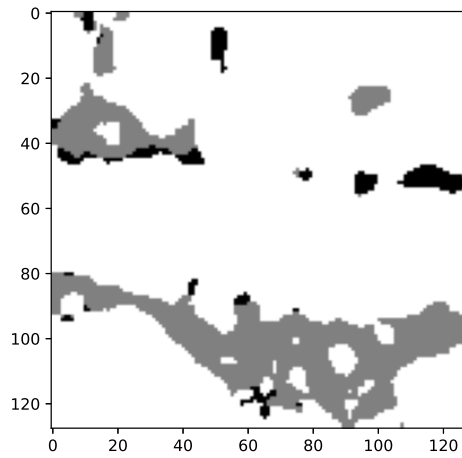
A Probing segmentation masks



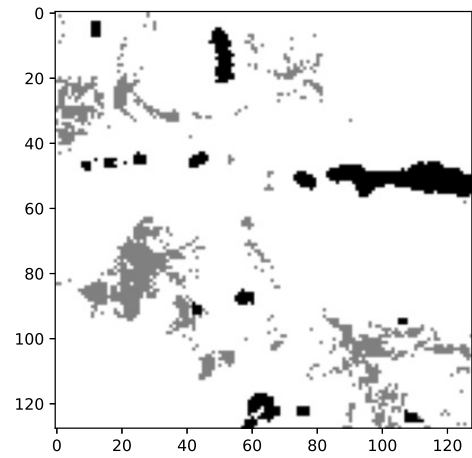
(a) CT-scanner



(b) GT



(c) DINOv2



(d) BFE

Figure 10: Prediction samples for kNN probing with DINOv2 and BFE as feature extractor.

B Benchmark segmentation masks

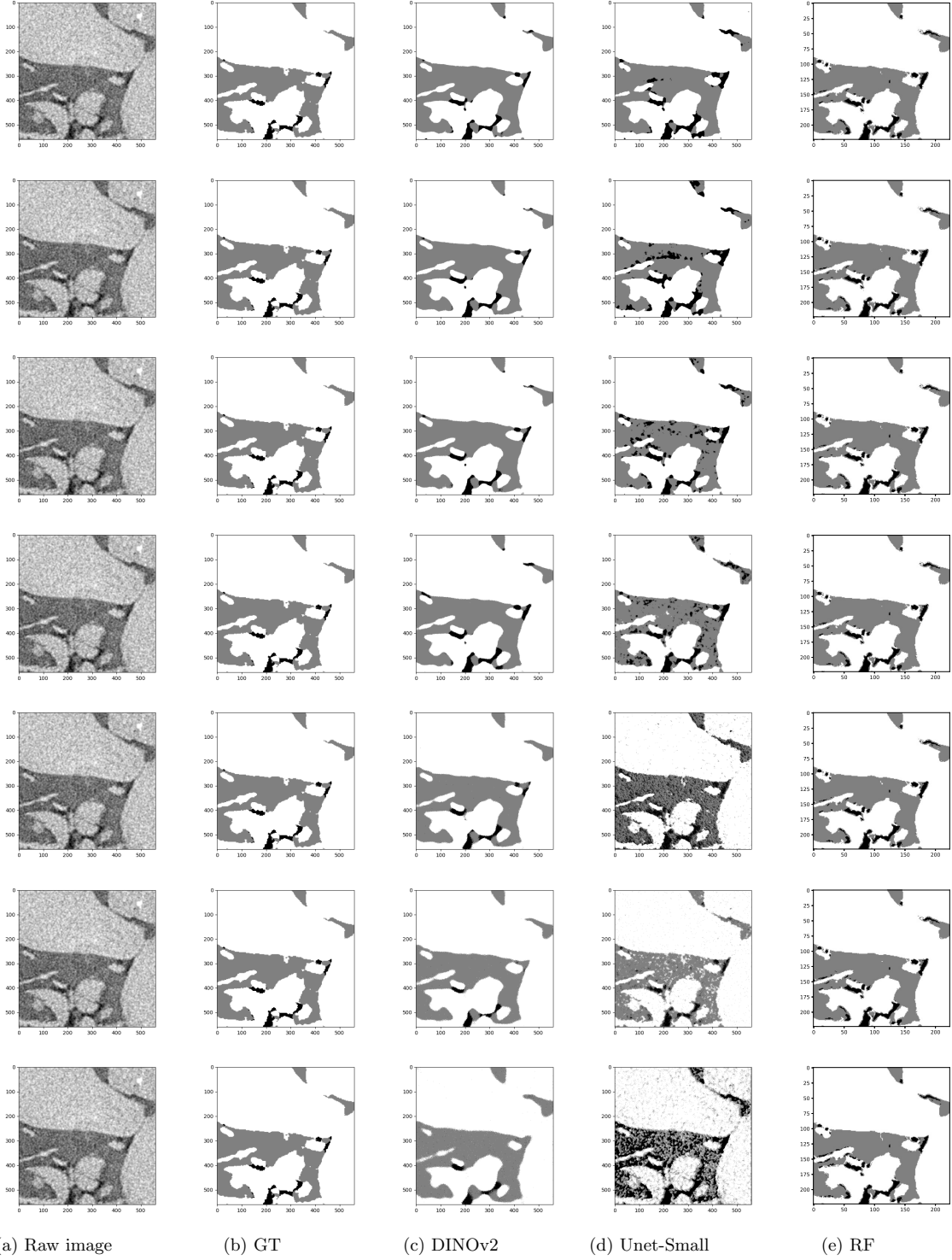


Figure 11: Predicted segmentation mask for DINOv2 (c), UNet-Small (d) and RF (e) as a function of the number of training samples, with 1000 training samples as the top row and 4 as the bottom row. The raw image (a) and the GT (b) are provided for comparison.

References

- [1] H. Al-Marzouqi. Digital rock physics: using ct scans to compute rock properties. *ieee signal process mag* 35: 121–131, 2018.
- [2] A. M. Alhammadi, A. AlRatrout, K. Singh, B. Bijeljic, and M. J. Blunt. In situ characterization of mixed-wettability in a reservoir rock at subsurface conditions. *Scientific reports*, 7(1):10753, 2017.
- [3] S. An, N. Wenck, S. Manoorkar, S. Berg, C. Taberner, R. Pini, and S. Krevor. Inverse modelling of core flood experiments for predictive models of sandstone and carbonate rocks. *Authorea Preprints*, 2023.
- [4] D. Anand, V. Singhal, D. D. Shanbhag, S. KS, U. Patil, C. Bhushan, K. Manickam, D. Gui, R. Mullick, A. Gopal, et al. One-shot localization and segmentation of medical images with foundation models. *arXiv preprint arXiv:2310.18642*, 2023.
- [5] I. Arganda-Carreras, V. Kaynig, C. Rueden, K. W. Eliceiri, J. Schindelin, A. Cardona, and H. Sebastian Seung. Trainable weka segmentation: a machine learning tool for microscopy pixel classification. *Bioinformatics*, 33(15):2424–2426, 2017.
- [6] M. Baharoon, W. Qureshi, J. Ouyang, Y. Xu, K. Phol, A. Aljouie, and W. Peng. Towards general purpose vision foundation models for medical image analysis: An experimental study of dinov2 on radiology benchmarks. *arXiv preprint arXiv:2312.02366*, 2023.
- [7] M. Balcewicz, M. Siegert, M. Gurriss, M. Ruf, D. Krach, H. Steeb, and E. H. Saenger. Digital rock physics: A geological driven workflow for the segmentation of anisotropic ruhr sandstone. *Frontiers in Earth Science*, 9:673753, 2021.
- [8] S. Belhassen and H. Zaidi. A novel fuzzy c-means algorithm for unsupervised heterogeneous tumor quantification in pet. *Medical physics*, 37(3):1309–1324, 2010.
- [9] R. Bensaid, V. Gripon, F. Leduc-Primeau, L. Mauch, G. B. Hacene, and F. Cardinaux. A novel benchmark for few-shot semantic segmentation in the era of foundation models. *arXiv preprint arXiv:2401.11311*, 2024.
- [10] S. Berg, N. Saxena, M. Shaik, and C. Pradhan. Generation of ground truth images to validate micro-ct image-processing pipelines. *The Leading Edge*, 37(6):412–420, 2018.
- [11] M. J. Blunt. *Multiphase flow in permeable media: A pore-scale perspective*. Cambridge university press, 2017.
- [12] X. Bou, G. Facciolo, R. G. Von Gioi, J.-M. Morel, and T. Ehret. Exploring robust features for few-shot object detection in satellite imagery. In *Proceedings of the IEEE/CVF Conference on Computer Vision and Pattern Recognition*, pages 430–439, 2024.
- [13] M. Bui, C. S. Adjiman, A. Bardow, E. J. Anthony, A. Boston, S. Brown, P. S. Fennell, S. Fuss, A. Galindo, L. A. Hackett, et al. Carbon capture and storage (ccs): the way forward. *Energy & Environmental Science*, 11(5):1062–1176, 2018.
- [14] V. I. Butoi, J. J. G. Ortiz, T. Ma, M. R. Sabuncu, J. Guttag, and A. V. Dalca. Universeg: Universal medical image segmentation. In *Proceedings of the IEEE/CVF International Conference on Computer Vision*, pages 21438–21451, 2023.
- [15] M. Caron, H. Touvron, I. Misra, H. Jégou, J. Mairal, P. Bojanowski, and A. Joulin. Emerging properties in self-supervised vision transformers, 2021.
- [16] Y. Chang. Improving the otsu method for mra image vessel extraction via resampling and ensemble learning. *Healthcare technology letters*, 6(4):115–120, 2019.
- [17] S. Chauhan, W. Rühaak, H. Anbergen, A. Kabdenov, M. Freise, T. Wille, and I. Sass. Phase segmentation of x-ray computer tomography rock images using machine learning techniques: an accuracy and performance study. *Solid Earth*, 7(4):1125–1139, 2016.

- [18] J. Chen, Y. Lu, Q. Yu, X. Luo, E. Adeli, Y. Wang, L. Lu, A. L. Yuille, and Y. Zhou. Transunet: Transformers make strong encoders for medical image segmentation. *arXiv preprint arXiv:2102.04306*, 2021.
- [19] R. J. Chen, T. Ding, M. Y. Lu, D. F. Williamson, G. Jaume, B. Chen, A. Zhang, D. Shao, A. H. Song, M. Shaban, et al. A general-purpose self-supervised model for computational pathology. *arXiv preprint arXiv:2308.15474*, 2023.
- [20] T. Chen, S. Kornblith, M. Norouzi, and G. Hinton. A simple framework for contrastive learning of visual representations. In *International conference on machine learning*, pages 1597–1607. PMLR, 2020.
- [21] Z. Chen, X. Liu, J. Yang, E. Little, and Y. Zhou. Deep learning-based method for sem image segmentation in mineral characterization, an example from duvernay shale samples in western canada sedimentary basin. *Computers & Geosciences*, 138:104450, 2020.
- [22] B. Cheng, I. Misra, A. G. Schwing, A. Kirillov, and R. Girdhar. Masked-attention mask transformer for universal image segmentation. In *Proceedings of the IEEE/CVF conference on computer vision and pattern recognition*, pages 1290–1299, 2022.
- [23] A. Cristóbal, X. Rigueira, I. Pérez-Rey, X. Estévez-Ventosa, M. Pazo, M. L. Napoli, B. X. Currás, and L. R. Alejano. Automatic characterization of block-in-matrix rock outcrops through segmentation algorithms and its application to an archaeo-mining case study. *Geosciences*, 14(2):29, 2024.
- [24] B. Cui, M. Islam, L. Bai, and H. Ren. Surgical-dino: adapter learning of foundation models for depth estimation in endoscopic surgery. *International Journal of Computer Assisted Radiology and Surgery*, pages 1–8, 2024.
- [25] Y. Da Wang, M. J. Blunt, R. T. Armstrong, and P. Mostaghimi. Deep learning in pore scale imaging and modeling. *Earth-Science Reviews*, 215:103555, 2021.
- [26] Y. Da Wang, M. Shabaninejad, R. T. Armstrong, and P. Mostaghimi. Deep neural networks for improving physical accuracy of 2d and 3d multi-mineral segmentation of rock micro-ct images. *Applied Soft Computing*, 104:107185, 2021.
- [27] T. Dettmers, A. Pagnoni, A. Holtzman, and L. Zettlemoyer. Qlora: Efficient finetuning of quantized llms. *Advances in Neural Information Processing Systems*, 36, 2024.
- [28] J. Dippel, B. Feulner, T. Winterhoff, S. Schallenberg, G. Dernbach, A. Kunft, S. Tietz, P. Jurmeister, D. Horst, L. Ruff, et al. Rudolfov: a foundation model by pathologists for pathologists. *arXiv preprint arXiv:2401.04079*, 2024.
- [29] H. Dong and M. J. Blunt. Pore-network extraction from micro-computerized-tomography images. *Physical review E*, 80(3):036307, 2009.
- [30] J. C. Dunn. A fuzzy relative of the isodata process and its use in detecting compact well-separated clusters. 1973.
- [31] G. Garfi, C. M. John, S. Berg, and S. Krevor. The sensitivity of estimates of multiphase fluid and solid properties of porous rocks to image processing. *Transport in Porous Media*, 131(3):985–1005, 2020.
- [32] I. Giannakis, A. Bhardwaj, L. Sam, and G. Leontidis. A flexible deep learning crater detection scheme using segment anything model (sam). *Icarus*, 408:115797, 2024.
- [33] J.-B. Grill, F. Strub, F. Altché, C. Tallec, P. Richemond, E. Buchatskaya, C. Doersch, B. Avila Pires, Z. Guo, M. Gheshlaghi Azar, et al. Bootstrap your own latent-a new approach to self-supervised learning. *Advances in neural information processing systems*, 33:21271–21284, 2020.
- [34] K. He, X. Zhang, S. Ren, and J. Sun. Deep residual learning for image recognition. In *Proceedings of the IEEE conference on computer vision and pattern recognition*, pages 770–778, 2016.

- [35] S. Henkel, D. Pudlo, L. Werner, F. Enzmann, V. Reitenbach, D. Albrecht, H. Würdemann, K. Heister, L. Ganzer, and R. Gaupp. Mineral reactions in the geological underground induced by h₂ and co₂ injections. *Energy Procedia*, 63:8026–8035, 2014.
- [36] E. J. Hu, Y. Shen, P. Wallis, Z. Allen-Zhu, Y. Li, S. Wang, L. Wang, and W. Chen. Lora: Low-rank adaptation of large language models. *arXiv preprint arXiv:2106.09685*, 2021.
- [37] Y. Hu, J. Wang, X. Wang, Y. Sun, H. Yu, and J. Zhang. Real-time evaluation of the blending uniformity of industrially produced gravelly soil based on cond-yolov8-seg. *Journal of Industrial Information Integration*, 39:100603, 2024.
- [38] Y. Huang, J. Zou, L. Meng, X. Yue, Q. Zhao, J. Li, C. Song, G. Jimenez, S. Li, and G. Fu. Comparative analysis of imagenet pre-trained deep learning models and dinov2 in medical imaging classification. *arXiv preprint arXiv:2402.07595*, 2024.
- [39] J. P. Huix, A. R. Ganeshan, J. F. Haslum, M. Söderberg, C. Matsoukas, and K. Smith. Are natural domain foundation models useful for medical image classification? In *Proceedings of the IEEE/CVF Winter Conference on Applications of Computer Vision*, pages 7634–7643, 2024.
- [40] E. R. Ibrahim, M. S. Jouini, F. Bouchaala, and J. Gomes. Simulation and validation of porosity and permeability of synthetic and real rock models using three-dimensional printing and digital rock physics. *ACS omega*, 6(47):31775–31781, 2021.
- [41] S. Iglaer, M. A. Fernø, P. Shearing, and M. J. Blunt. Comparison of residual oil cluster size distribution, morphology and saturation in oil-wet and water-wet sandstone. *Journal of colloid and interface science*, 375(1):187–192, 2012.
- [42] A. K. Jain. Data clustering: 50 years beyond k-means. *Pattern recognition letters*, 31(8):651–666, 2010.
- [43] N. K. Jha, A. Al-Yaseri, M. Ghasemi, D. Al-Bayati, M. Lebedev, and M. Sarmadivaleh. Pore scale investigation of hydrogen injection in sandstone via x-ray micro-tomography. *International Journal of Hydrogen Energy*, 46(70):34822–34829, 2021.
- [44] M. Jouini, F. Bouchaala, E. Ibrahim, and F. Hjouj. Permeability and porosity upscaling method using machine learning and digital rock physics. In *83rd EAGE Annual Conference & Exhibition*, volume 2022, pages 1–5. European Association of Geoscientists & Engineers, 2022.
- [45] S. Julka and M. Granitzer. Knowledge distillation with segment anything (sam) model for planetary geological mapping. In *International Conference on Machine Learning, Optimization, and Data Science*, pages 68–77. Springer, 2023.
- [46] A. Kirillov, E. Mintun, N. Ravi, H. Mao, C. Rolland, L. Gustafson, T. Xiao, S. Whitehead, A. C. Berg, W.-Y. Lo, P. Dollár, and R. Girshick. Segment anything, 2023.
- [47] A. Koeshidayatullah. Riding the wave: One-touch automatic salt segmentation by coupling sam and seggpt. In *Abu Dhabi International Petroleum Exhibition and Conference*, page D021S053R002. SPE, 2023.
- [48] S. Krevor and B. Niu. The impact of mineral dissolution on multiphase flow in permeable carbonates. In *AGU Fall Meeting Abstracts*, volume 2015, pages H23D–1613, 2015.
- [49] S. C. Krevor, S. J. Jackson, and S. Agada. Core analysis of heterogeneous rocks using experimental observations and digital whole core simulation. In *2017 AGU Fall Meeting*. AGU, 2017.
- [50] Y. LeCun, B. Boser, J. S. Denker, D. Henderson, R. E. Howard, W. Hubbard, and L. D. Jackel. Backpropagation applied to handwritten zip code recognition. *Neural computation*, 1(4):541–551, 1989.
- [51] Y. Lee, A. S. Chen, F. Tajwar, A. Kumar, H. Yao, P. Liang, and C. Finn. Surgical fine-tuning improves adaptation to distribution shifts. In *The Eleventh International Conference on Learning Representations*, 2023.

- [52] C. Li, D. Wang, and L. Kong. Application of machine learning techniques in mineral classification for scanning electron microscopy-energy dispersive x-ray spectroscopy (sem-eds) images. *Journal of Petroleum Science and Engineering*, 200:108178, 2021.
- [53] J. Liang, Y. Sun, M. Lebedev, B. Gurevich, M. Nzikou, S. Vialle, and S. Glubokovskikh. Multi-mineral segmentation of micro-tomographic images using a convolutional neural network. *Computers & Geosciences*, 168:105217, 2022.
- [54] P.-S. Liao, T.-S. Chen, P.-C. Chung, et al. A fast algorithm for multilevel thresholding. *J. Inf. Sci. Eng.*, 17(5):713–727, 2001.
- [55] A. Liaw, M. Wiener, et al. Classification and regression by randomforest. *R news*, 2(3):18–22, 2002.
- [56] L. Liu, Q. Han, Y. Zhao, and Y. Zhao. A novel method combining u-net with lstm for three-dimensional soil pore segmentation based on computed tomography images. *Applied Sciences*, 14(8):3352, 2024.
- [57] C. Lormand, G. F. Zellmer, K. Németh, G. Kilgour, S. Mead, A. S. Palmer, N. Sakamoto, H. Yurimoto, and A. Moebis. Weka trainable segmentation plugin in imagej: a semi-automatic tool applied to crystal size distributions of microlites in volcanic rocks. *Microscopy and Microanalysis*, 24(6):667–675, 2018.
- [58] Z. Ma, X. He, S. Sun, B. Yan, H. Kwak, and J. Gao. Zero-shot digital rock image segmentation with a fine-tuned segment anything model. *arXiv preprint arXiv:2311.10865*, 2023.
- [59] J. MacQueen et al. Some methods for classification and analysis of multivariate observations. In *Proceedings of the fifth Berkeley symposium on mathematical statistics and probability*, volume 1, pages 281–297. Oakland, CA, USA, 1967.
- [60] A. Mahmoud, R. Gajbhiye, J. Li, J. Dvorkin, S. R. Hussaini, and H. S. AlMukainah. Digital rock physics (drp) workflow to assess reservoir flow characteristics. *Arabian Journal of Geosciences*, 16(4):248, 2023.
- [61] I. Main, M.-D. Mangriotis, A. Cartwright-Taylor, A. Curtis, I. Butler, A. Bell, and F. Fusseis. Progressive rock failure under different loading conditions—sound and vision. Technical report, Copernicus Meetings, 2024.
- [62] O. A. Malik, I. Puasa, and D. T. C. Lai. Segmentation for multi-rock types on digital outcrop photographs using deep learning techniques. *Sensors*, 22(21):8086, 2022.
- [63] Y. Mansour and M. Schain. Learning with maximum-entropy distributions. *Machine Learning*, 45:123–145, 2001.
- [64] S. Manzoor, T. Qasim, N. Bhatti, and M. Zia. Segmentation of digital rock images using texture analysis and deep network. *Arabian Journal of Geosciences*, 16(7):436, 2023.
- [65] P. Mostaghimi, B. Bijeljic, and M. J. Blunt. Simulation of flow and dispersion on pore-space images. *SPE Journal*, 17(04):1131–1141, 2012.
- [66] M. Mounsif, Y. Motie, M. Benabdelkrim, and F. Brondolo. Synfine: Boosting image segmentation accuracy through synthetic data generation and surgical fine-tuning. In *ICPRAM*, pages 565–573, 2023.
- [67] R. F. Neumann, M. Barsi-Andreetta, E. Lucas-Oliveira, H. Barbalho, W. A. Trevizan, T. J. Bonagamba, and M. B. Steiner. High accuracy capillary network representation in digital rock reveals permeability scaling functions. *Scientific reports*, 11(1):11370, 2021.
- [68] Y. Niu, P. Mostaghimi, M. Shabaninejad, P. Swietojanski, and R. T. Armstrong. Digital rock segmentation for petrophysical analysis with reduced user bias using convolutional neural networks. *Water Resources Research*, 56(2):e2019WR026597, 2020.

- [69] M. Oquab, T. Darcet, T. Moutakanni, H. Vo, M. Szafraniec, V. Khalidov, P. Fernandez, D. Haziza, F. Massa, A. El-Nouby, M. Assran, N. Ballas, W. Galuba, R. Howes, P.-Y. Huang, S.-W. Li, I. Misra, M. Rabbat, V. Sharma, G. Synnaeve, H. Xu, H. Jegou, J. Mairal, P. Labatut, A. Joulin, and P. Bojanowski. Dinov2: Learning robust visual features without supervision, 2024.
- [70] N. Otsu et al. A threshold selection method from gray-level histograms. *Automatica*, 11(285-296):23–27, 1975.
- [71] T. Pak, I. B. Butler, S. Geiger, M. I. Van Dijke, and K. S. Sorbie. Droplet fragmentation: 3d imaging of a previously unidentified pore-scale process during multiphase flow in porous media. *Proceedings of the National Academy of Sciences*, 112(7):1947–1952, 2015.
- [72] F. Pérez-García, H. Sharma, S. Bond-Taylor, K. Bouzid, V. Salvatelli, M. Ilse, S. Bannur, D. C. Castro, A. Schwaighofer, M. P. Lungren, et al. Rad-dino: Exploring scalable medical image encoders beyond text supervision. *arXiv preprint arXiv:2401.10815*, 2024.
- [73] C. Pham, L. Zhuang, S. Yeom, and H.-S. Shin. Automatic fracture characterization in ct images of rocks using an ensemble deep learning approach. *International Journal of Rock Mechanics and Mining Sciences*, 170:105531, 2023.
- [74] P. Purswani, Z. T. Karpyn, K. Enab, Y. Xue, and X. Huang. Evaluation of image segmentation techniques for image-based rock property estimation. *Journal of Petroleum Science and Engineering*, 195:107890, 2020.
- [75] A. Radford, J. W. Kim, C. Hallacy, A. Ramesh, G. Goh, S. Agarwal, G. Sastry, A. Askell, P. Mishkin, J. Clark, G. Krueger, and I. Sutskever. Learning transferable visual models from natural language supervision, 2021.
- [76] M. Reinhardt, A. Jacob, S. Sadeghnejad, F. Cappuccio, P. Arnold, S. Frank, F. Enzmann, and M. Kersten. Benchmarking conventional and machine learning segmentation techniques for digital rock physics analysis of fractured rocks. *Environmental Earth Sciences*, 81(3):71, 2022.
- [77] O. Ronneberger, P. Fischer, and T. Brox. U-net: Convolutional networks for biomedical image segmentation. In *Medical image computing and computer-assisted intervention–MICCAI 2015: 18th international conference, Munich, Germany, October 5-9, 2015, proceedings, part III 18*, pages 234–241. Springer, 2015.
- [78] R. Rulaningtyas, K. Ain, et al. Ct scan image segmentation based on hounsfield unit values using otsu thresholding method. In *Journal of Physics: Conference Series*, volume 1816, page 012080. IOP Publishing, 2021.
- [79] J. Schindelin, I. Arganda-Carreras, E. Frise, V. Kaynig, M. Longair, T. Pietzsch, S. Preibisch, C. Rueden, S. Saalfeld, B. Schmid, et al. Fiji: an open-source platform for biological-image analysis. *Nature methods*, 9(7):676–682, 2012.
- [80] L. Shan, Y. Liu, K. Du, S. Paul, X. Zhang, and X. Hei. Drilling rock image segmentation and analysis using segment anything model. *Advances in Geo-Energy Research*, 12(2), 2024.
- [81] S. Shankar, L. A. Stearns, and C. van der Veen. Semantic segmentation of glaciological features across multiple remote sensing platforms with the segment anything model (sam). *Journal of Glaciology*, pages 1–10, 2023.
- [82] L. Shapiro and G. Stockman. Computer vision prentice hall. *Inc., New Jersey*, page 552, 2001.
- [83] Y. Song, Z. Huang, C. Shen, H. Shi, and D. A. Lange. Deep learning-based automated image segmentation for concrete petrographic analysis. *Cement and Concrete Research*, 135:106118, 2020.
- [84] A. B. Tatomir, M. Halisch, F. Duschl, A. Peche, B. Wiegand, M. Schaffer, T. Licha, A. Niemi, J. Bensabat, and M. Sauter. An integrated core-based analysis for the characterization of flow, transport and mineralogical parameters of the heletz pilot co2 storage site reservoir. *International Journal of Greenhouse Gas Control*, 48:24–43, 2016.

- [85] S. Tayebi Arasteh, L. Misera, J. N. Kather, D. Truhn, and S. Nebelung. Enhancing diagnostic deep learning via self-supervised pretraining on large-scale, unlabeled non-medical images. *European Radiology Experimental*, 8(1):10, 2024.
- [86] A. Vaswani, N. Shazeer, N. Parmar, J. Uszkoreit, L. Jones, A. N. Gomez, L. Kaiser, and I. Polosukhin. Attention is all you need. *Advances in neural information processing systems*, 30, 2017.
- [87] E. Vorontsov, A. Bozkurt, A. Casson, G. Shaikovski, M. Zelechowski, S. Liu, P. Mathieu, A. van Eck, D. Lee, J. Viret, et al. Virchow: a million-slide digital pathology foundation model. *arXiv preprint arXiv:2309.07778*, 2023.
- [88] I. Watt, I. Butler, F. Füsseis, I. Molnar, J. Gilgannon, S. Haszeldine, and S. Gilfillan. Lab-based assessment of engineered co2 mineralization in mafic rock reservoirs. Technical report, Copernicus Meetings, 2024.
- [89] Y. Wu and S. Misra. Intelligent image segmentation for organic-rich shales using random forest, wavelet transform, and hessian matrix. *IEEE Geoscience and Remote Sensing Letters*, 17(7):1144–1147, 2019.
- [90] E. Xie, W. Wang, Z. Yu, A. Anandkumar, J. M. Alvarez, and P. Luo. Segformer: Simple and efficient design for semantic segmentation with transformers. *Advances in neural information processing systems*, 34:12077–12090, 2021.
- [91] Z. Xu, W. Ma, P. Lin, H. Shi, D. Pan, and T. Liu. Deep learning of rock images for intelligent lithology identification. *Computers & Geosciences*, 154:104799, 2021.
- [92] P. Zhang, S. Lu, J. Li, P. Zhang, L. Xie, H. Xue, and J. Zhang. Multi-component segmentation of x-ray computed tomography (ct) image using multi-otsu thresholding algorithm and scanning electron microscopy. *Energy Exploration & Exploitation*, 35(3):281–294, 2017.
- [93] E. Zimmermann, N. Tenenholtz, J. Hall, G. Shaikovski, M. Zelechowski, A. Casson, F. Milletari, J. Viret, E. Vorontsov, S. Liu, et al. Adapting self-supervised learning for computational pathology. *arXiv preprint arXiv:2405.01688*, 2024.